Supplemental of

Measurements and modeling of urban secondary organic aerosol as a function of precursor volatility class in the Los Angeles area during summer 2022

Melissa Ehrenfels et al.

Correspondence to: Jose L. Jimenez (jose.jimenez@colorado.edu)

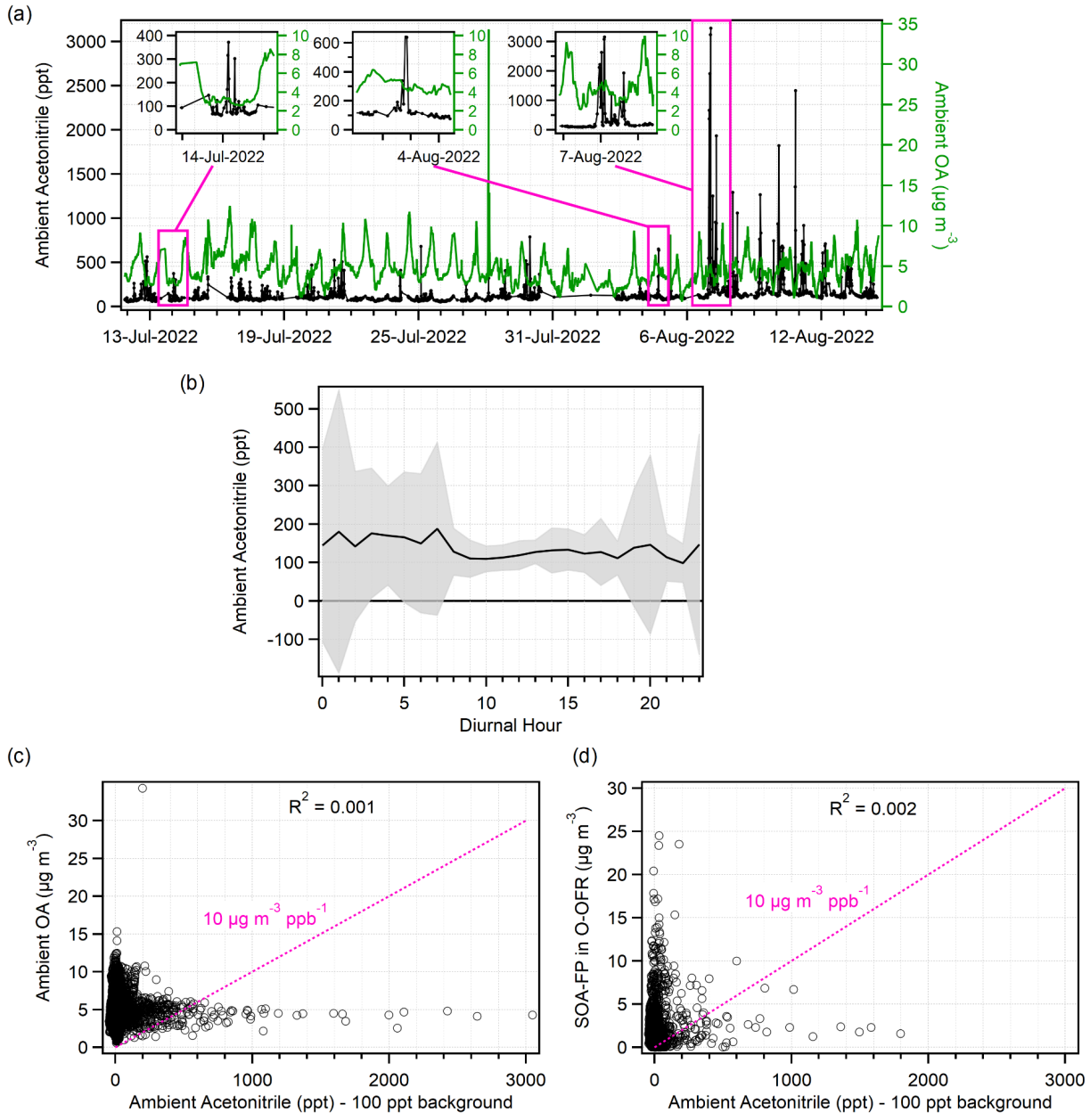

Figure S1. (a) A time series of measured ambient acetonitrile and ambient organic aerosol, with insets zoomed in to several acetonitrile spikes. (b) A campaign average diurnal of measured acetonitrile, with 1 standard deviation shown in grey. (c) Ambient organic aerosol vs ambient acetonitrile that has been background subtracted. A typical biomass burning organic aerosol to acetonitrile ratio from the literature is shown as a pink line (Aiken et al., 2010). Given the lack of correlation between acetonitrile and OA, we conclude that acetonitrile is arising from non-biomass burning sources in this campaign, and that the biomass burning influence on OA is very low. (d) Secondary organic aerosol formation potential in the O-OFR vs ambient acetonitrile that has been background subtracted, leading to similar conclusions.

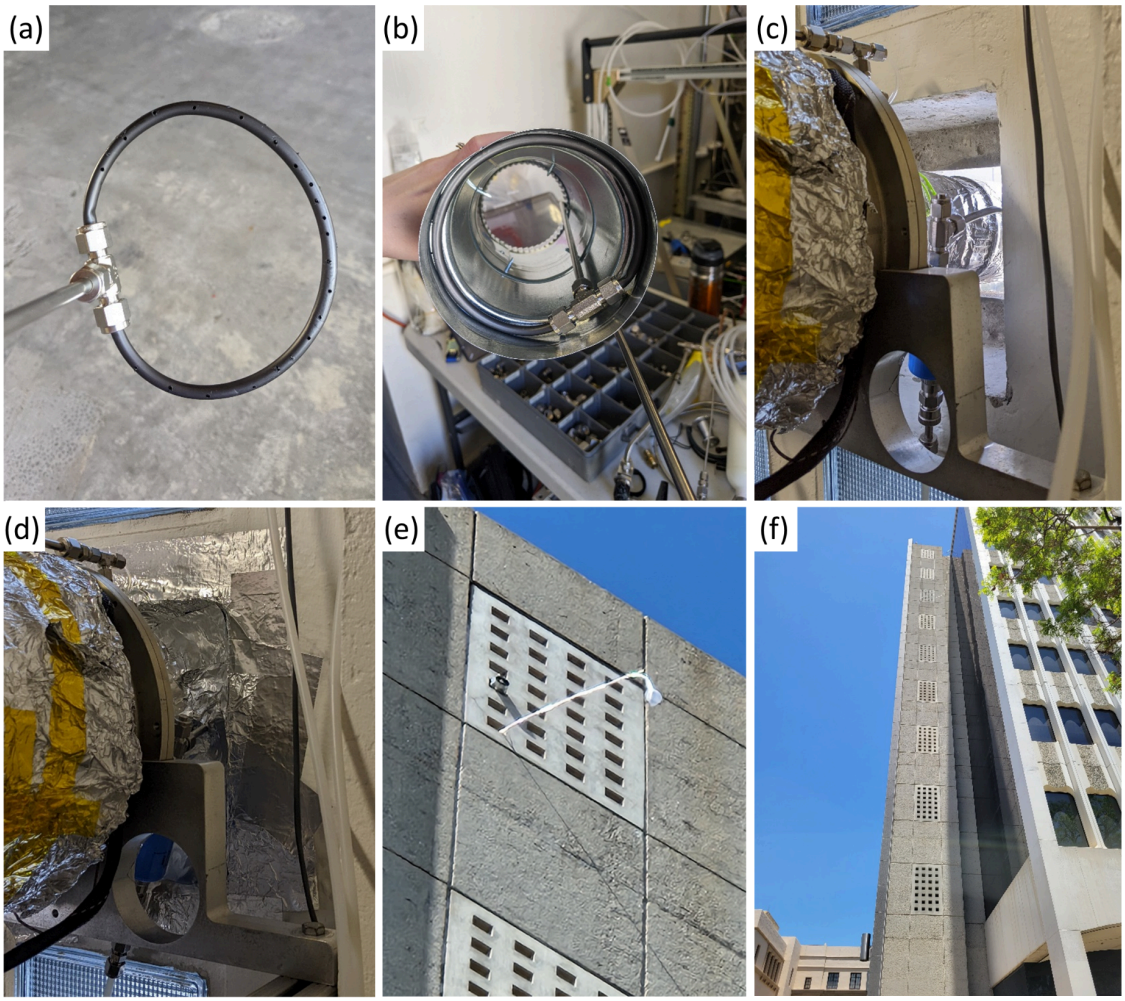

Figure S2. The O-OFR needed to sample air outside the concrete port, so a metal cone system was developed to seal it off from the indoor air and from wall effects from the concrete. (a) A custom vacuum line (made of electrically conductive PFA tubing) was built to remove any air from the ambient stream that had come in contact with the walls of the metal cone. (b) The custom vacuum line was installed close to the O-OFR face and the plumbing was routed out the front and around the metal cone. The flow rate through the vacuum port was nominally 3.5 LPM. (c) The metal cone was sealed to the O-OFR face using aluminum foil and aluminum foil tape. Careful attention was made so adhesive from the tape was never in contact with the sample stream. The seal on the cone was leak checked using CO_2 measurements throughout the campaign. (d) The O-OFR was sealed off from the room using the same aluminum foil and aluminum foil taping technique. (e) A zoomed in photo of the O-OFR metal cone from the outside, with the Vocus sampling line underneath. (f) A zoomed out version of photo E to show the height of the sampling.

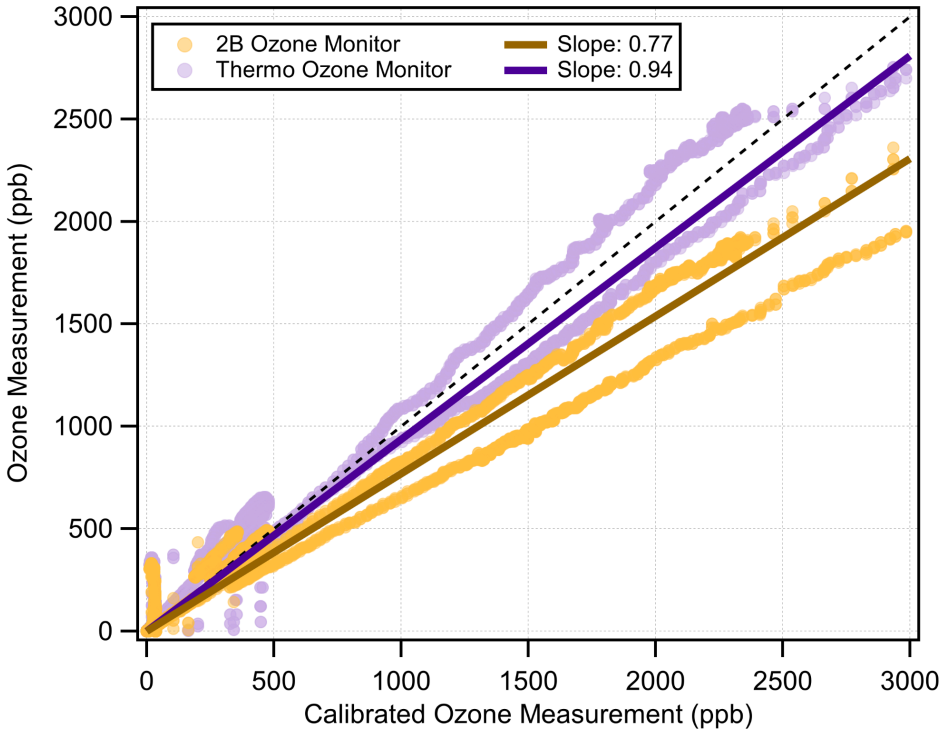

Figure S3. Prior to the campaign, the two field ozone instruments were compared to a third, calibrated ozone measurement (Thermo Scientific, Model 49i) in the laboratory. All three ozone instruments sampled the same OFR as the lights were ramped to produce ozone. The data appears as two lines per instrument, one for increasing ozone concentration and one for decreasing ozone concentration during the experiment; the average of all data was taken for the reported slopes. The slopes were used to correct the ozone data collected in the field. When applied, these corrections only changed the estimation of OH exposure from the estimation equation shown in Fig. S18. Analysis of toluene decay in each OFR was calculated to replace the results from the estimation equation.

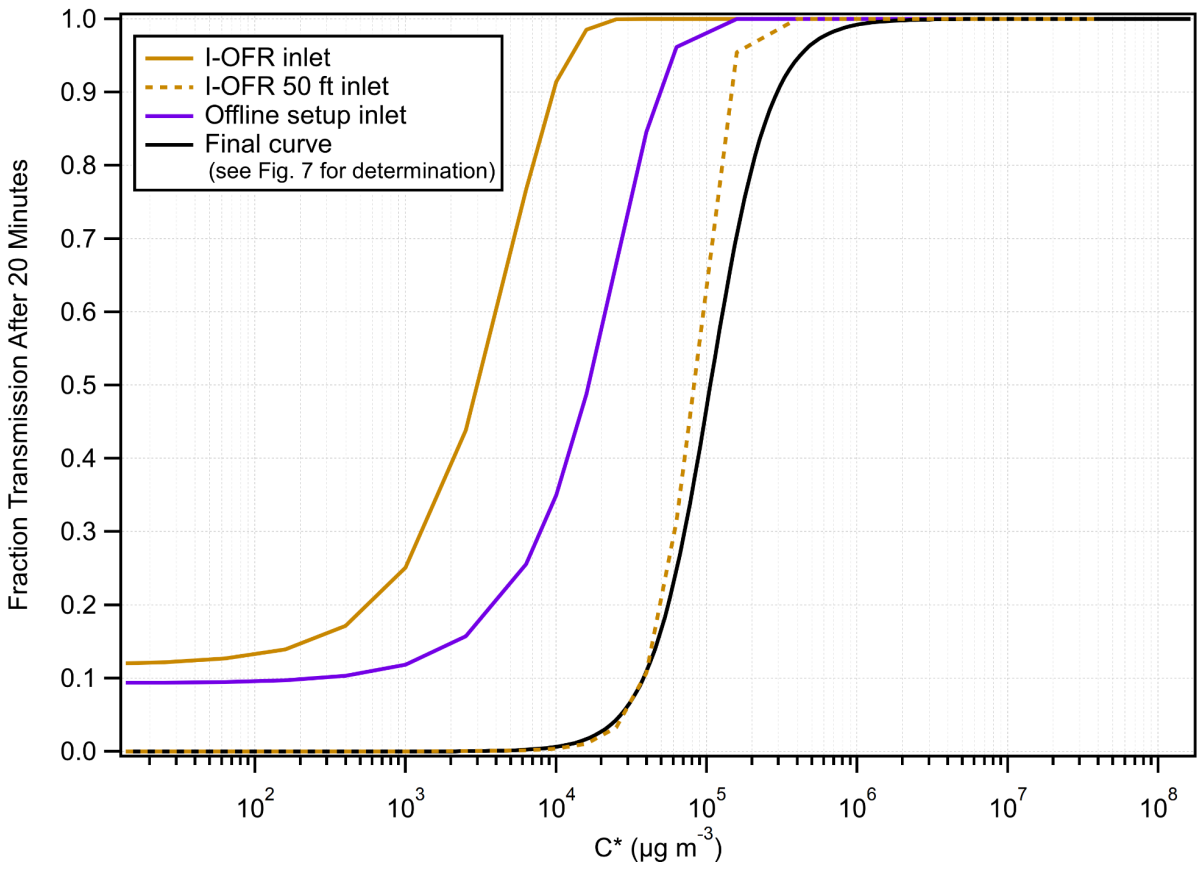

Figure S4. The tubing model published in Pagonis et al. (2017) was used to simulate several inlets: the predominant I-OFR inlet (cPFA, 3.5 m long, ¼" OD), a longer test I-OFR inlet (cPFA, 15 m long, ¼" OD) and the inlet used for the offline setup (PTFE, 1.5 m long, ¼" OD). Importantly, this prediction is only for the polymer tubing in the sampling setups. The sampled gas stream for the I-OFR also passed through 2 Teflon solenoid valves. The sampled gas stream for the offline setup also passed through a PTFE filter for particulate matter. Both of these are expected to increase the denuding of the sampling systems. We note that the shorter modeled tubes do not denude lower volatility species. This is because not all air touches the walls of the tubing in the model, which is assumed to be perfectly straight. In reality, our experimental setup included many bends, which would increase air mixing. Additionally, the model is only valid under a laminar flow regime, which we were at the upper limit of. See Fig. 3 for an experimental determination of the transmission curve for this work.

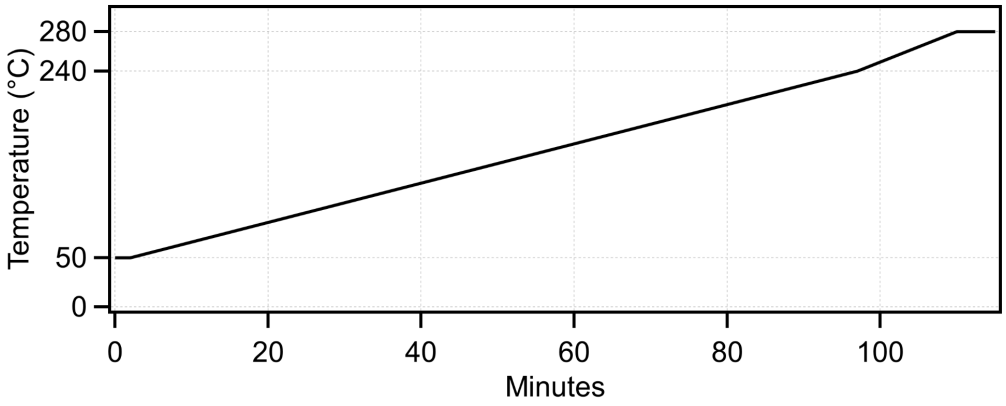

Figure. S5. Temperature ramp used for the cartridge analysis at Riverside.

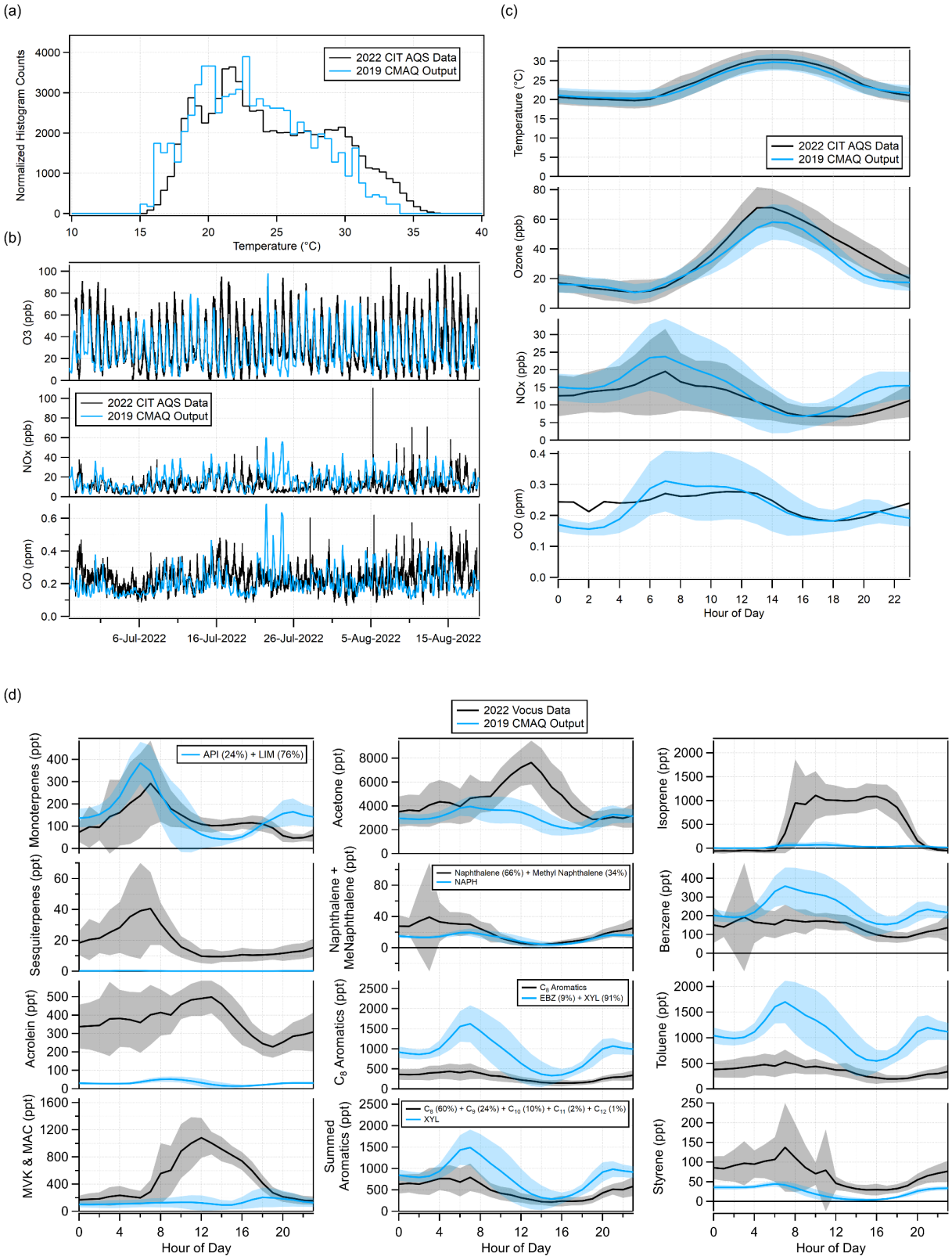
(a)
Normalized Histogram Counts
Temperature (°C)
2022 CIT AQS Data
2019 CMAQ Output
(b)
O3 (ppb)
NOx (ppb)
CO (ppm)
6-Jul-2022
16-Jul-2022
26-Jul-2022
5-Aug-2022
15-Aug-2022
(c)
Temperature (°C)
Ozone (ppb)
NOx (ppb)
CO (ppm)
Hour of Day
(d)
2022 Vocus Data
2019 CMAQ Output
API (24%) + LIM (76%)
Monoterpenes (ppt)
Sesquiterpenes (ppt)
Acrolein (ppt)
MVK & MAC (ppt)
Acetone (ppt)
Naphthalene (66%) + Methyl Naphthalene (34%)
NAPH
Naphthalene + MeNaphthalene (ppt)
C8 Aromatics
EBZ (9%) + XYL (91%)
C8 Aromatics (ppt)
C9 (60%) + C9 (24%) + C10 (10%) + C11 (2%) + C12 (1%)
XYL
Summed Aromatics (ppt)
Isoprene (ppt)
Benzene (ppt)
Toluene (ppt)
Styrene (ppt)
Hour of Day

Figure S6. Comparison of temperature, ozone, NO_x, CO and gas phase precursors between the measured data (2022) and model results (2019). CITAQS is the Caltech air quality system. (a) Normalized histograms of temperature. (b) Time series of ozone, NO_x and CO. (c) Diurnals of temperature, ozone, NO_x and CO. (d) Diurnal comparisons of gas phase precursors.

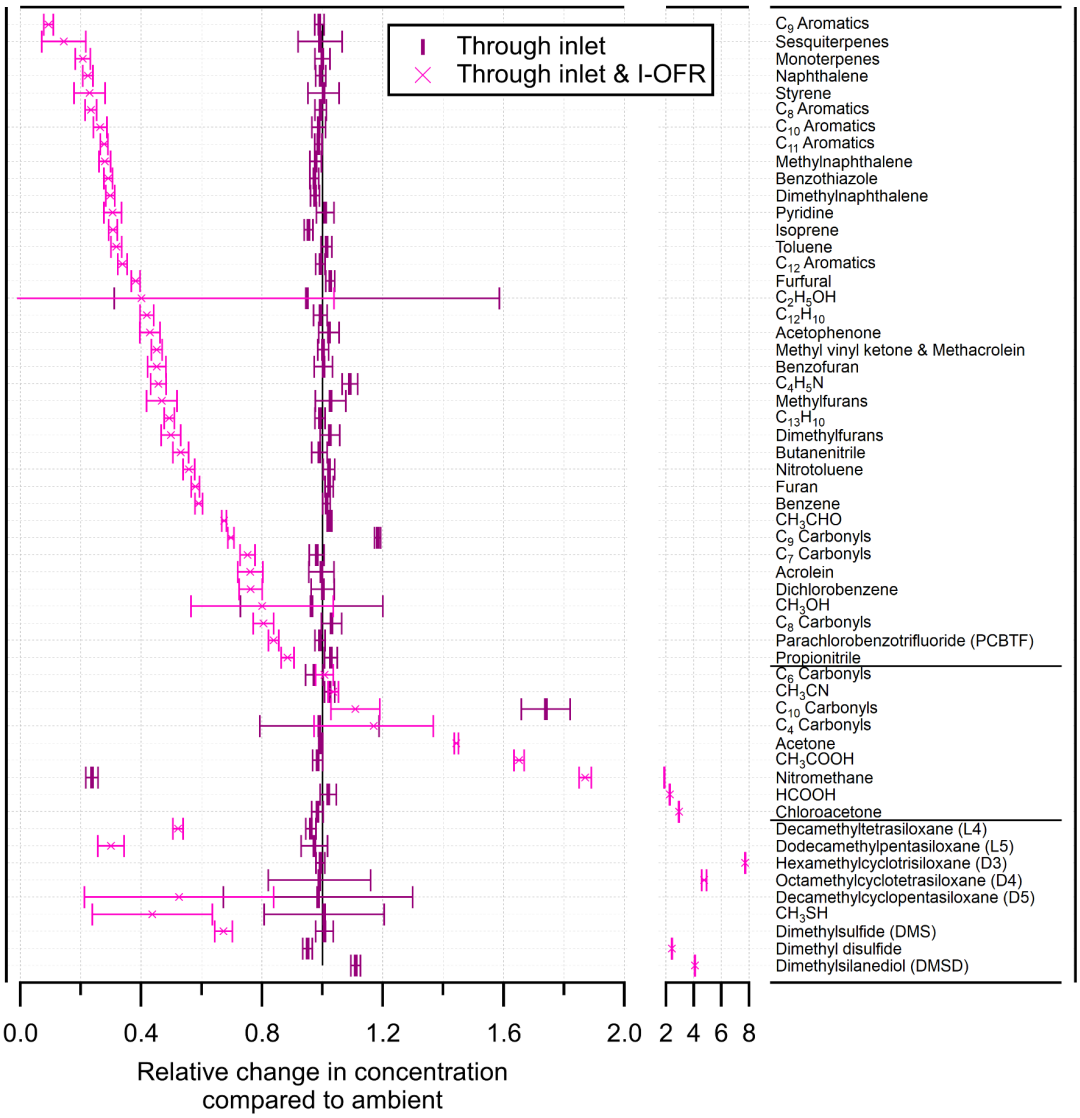

Figure S7. Fraction transmission of all gas-phase species measured by the Vocus through just the inlet of the I-OFR or the inlet and I-OFR combined. When measured through the I-OFR, some species decay due to oxidation (top category), while other species are enhanced because they are oxidation products (middle category). The bottom category contains sulfur-containing and siloxane species. A few species (C_9 carbonyls 54 ppt ambient average; C_{10} carbonyls 24 ppt; DMSD 68 ppt) show increases through the tubing, for reasons that are unclear. In any case their contribution to SOA-FP should be minimal.

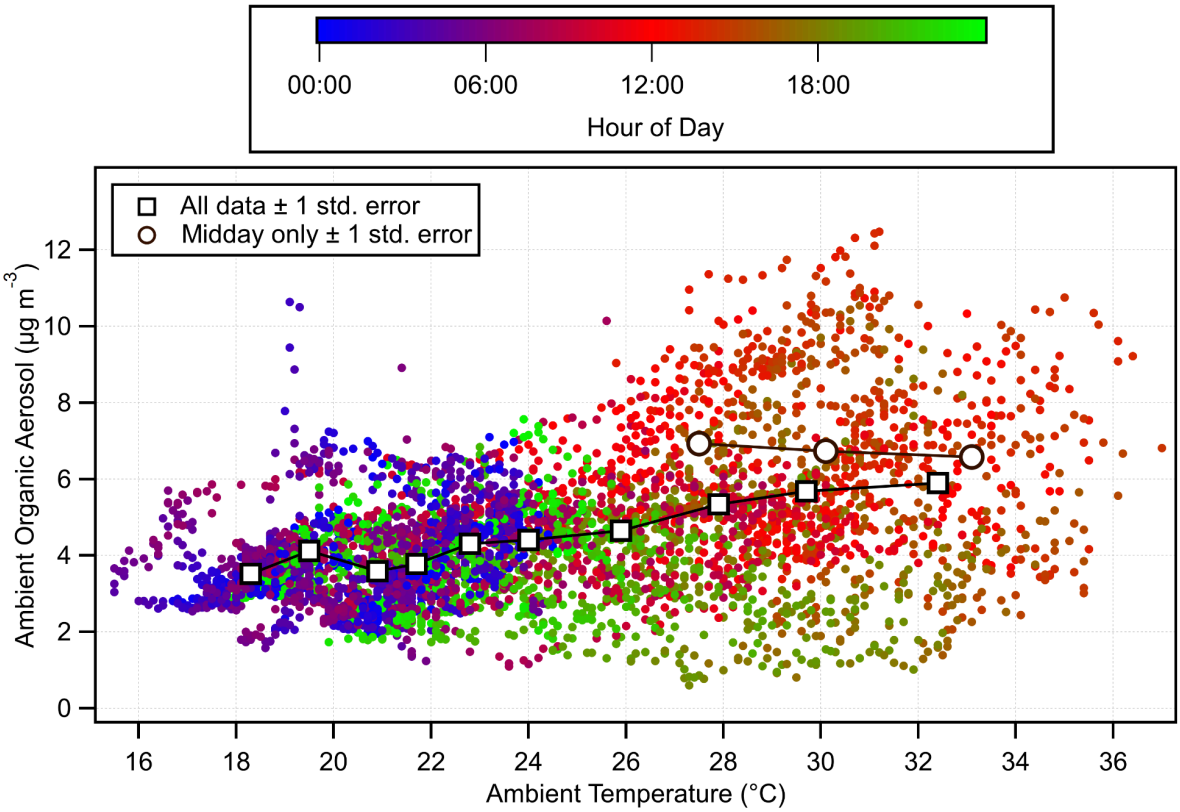

Figure S8. Measured ambient organic aerosol vs ambient temperature, colored by time of day. Quantiles of all data and midday only (11:00-16:00) are shown with vertical error bars being the std. error. All error bars are smaller than the markers.

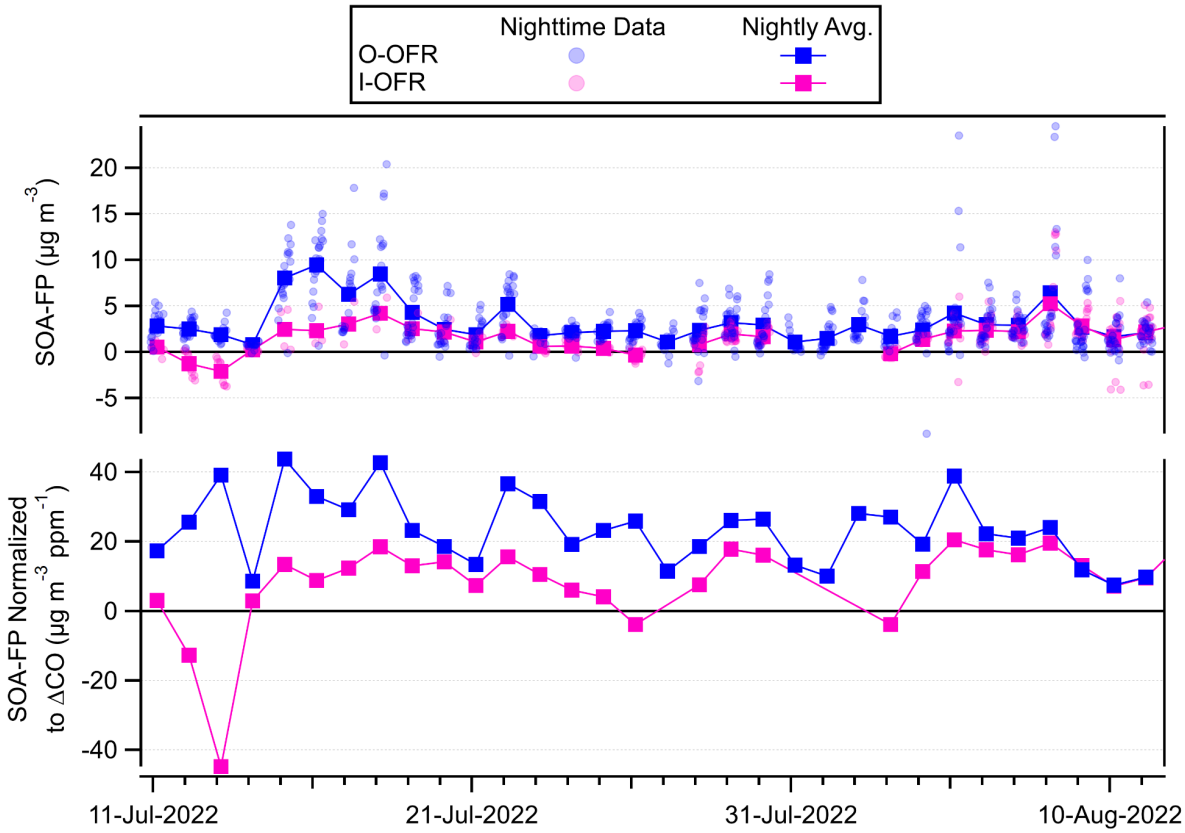

Figure S9. Top: Nighttime data and nightly average of SOA-FP. Bottom: Nightly averages normalized to average background-subtracted CO concentrations.

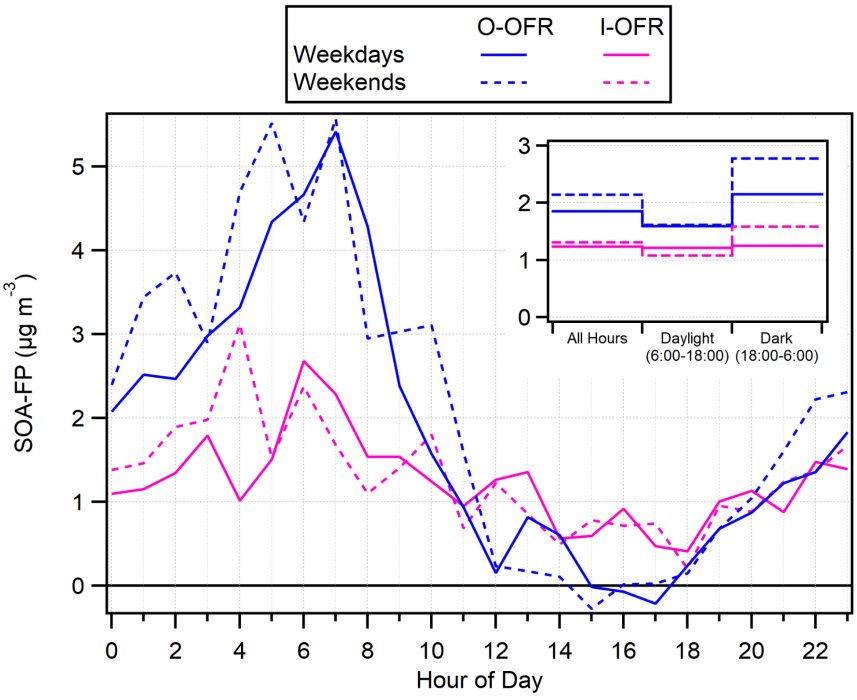

Figure S10. The campaign-average diurnal of SOA-FP measured in each OFR from Fig. 6 split between weekdays and weekends. An inset bar chart shows averages for specified time ranges.

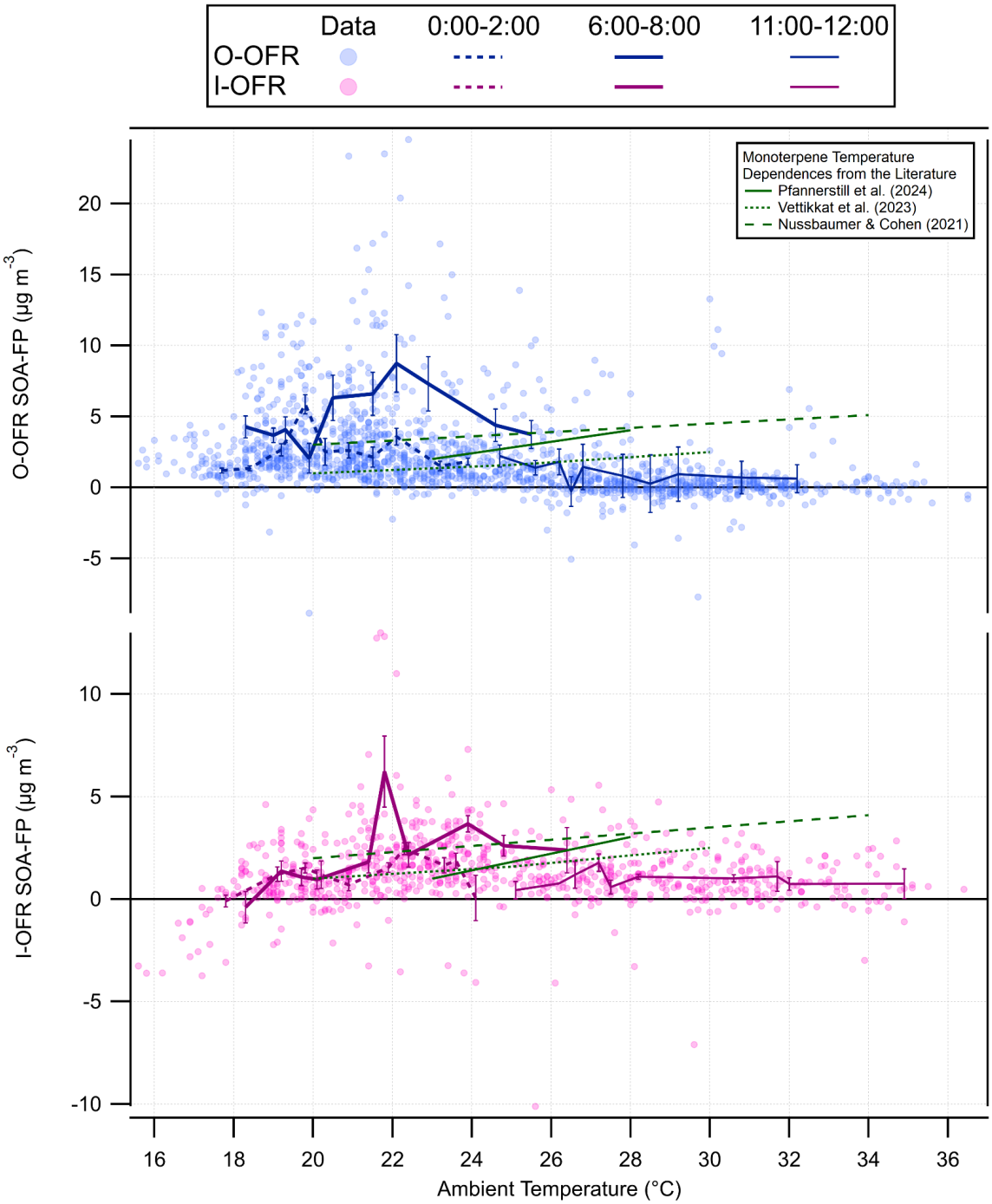

Figure S11. Measured SOA-FP for both OFRs according to ambient temperature. Deciles for the described time periods are shown as lines, with vertical error bars as the standard error. Some outlying data points are outside the y-axis ranges so that trends can be better analyzed visually. The green lines show relative expected SOA-FP enhancements from the literature for monoterpenes (Nussbaumer and Cohen, 2021; Pfannerstill et al., 2024; Vettikkat et al., 2023). The relative slope was calculated from the literature and added with an arbitrary y-offset for ease of visual comparison.

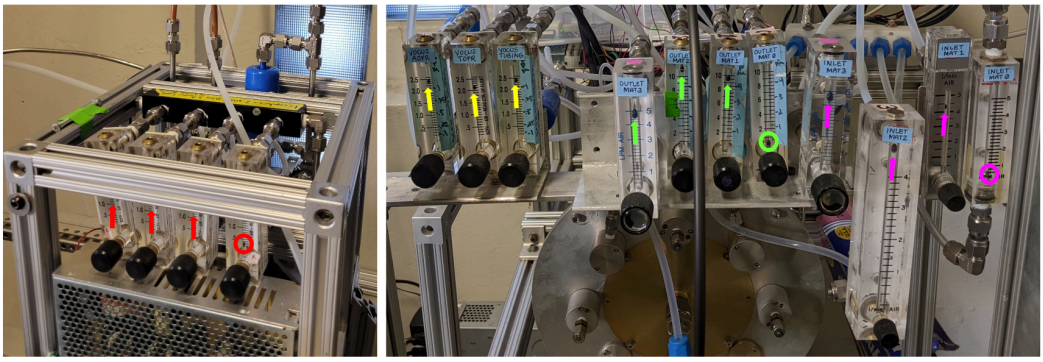

Figure S12. There were 15 rotameters installed in the system that could be read to understand how air was flowing. No rotameters were installed in the critical sampling path - all rotameters were installed on exhaust ports and zero air intakes. The red rotameters indicate which sampling pathway the aerosol instruments were measuring. Since 3 options were flowing to exhaust, the fourth option (ambient air) was being sampled. The yellow marked rotameters indicate which sampling pathway the gas instruments were measuring. Since all OFR-related options were flowing to exhaust, the system was sampling ambient air. The pink and green rotameters show if zero air is flowing to the I-OFR inlets and if the air through those inlets is being exhausted, respectively. In the photo, inlets 1-3 have zero air flowing through them to the exhaust, and inlet 0 is being sampled by the I-OFR.

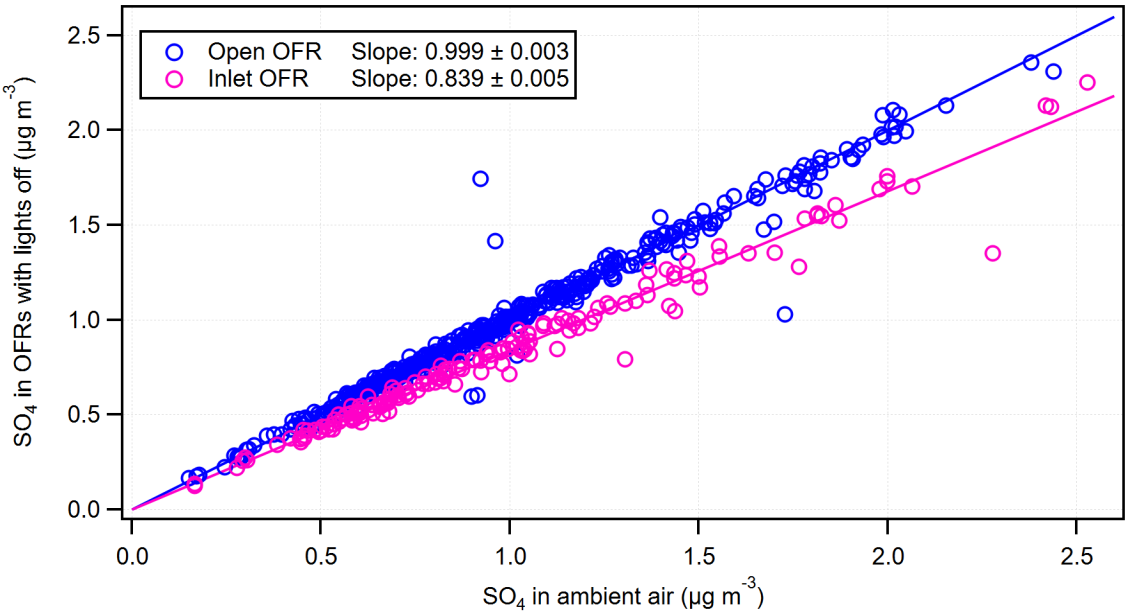

Figure S13. Correlation of SO_4 in the OFRs during periods where the lights were turned off, plotted against SO_4 in ambient air. Since the O-OFR had a slope of ~1, no correction for aerosol transmission was needed compared to the ambient inlet. Since the I-OFR had a slope of 0.839, the I-OFR OA values were corrected according to Eq. 1.

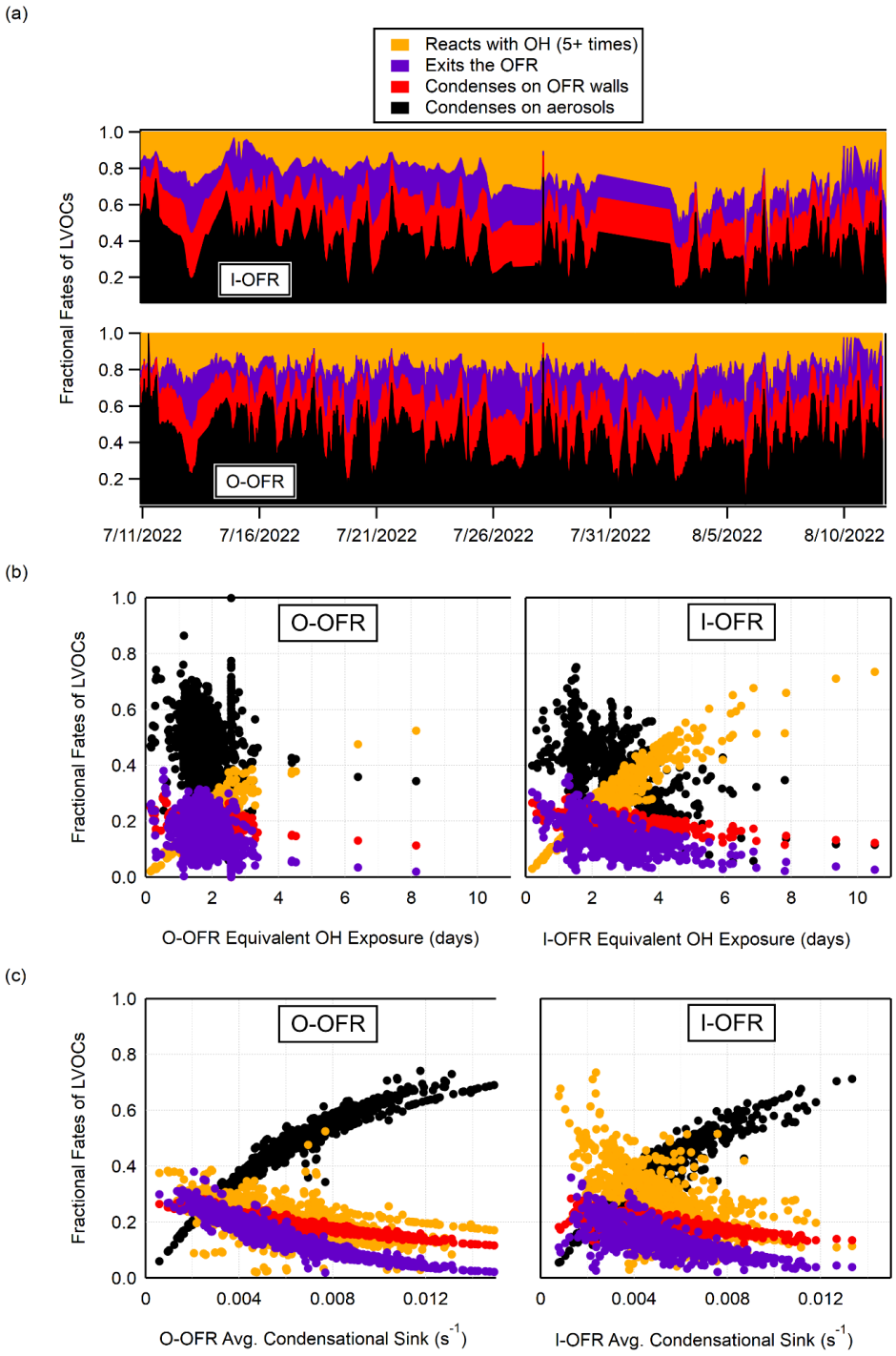

Figure S14. Results from the LVOC loss calculator for both OFRs (Palm et al., 2016). (a) Time series of fractional LVOC fates through various pathways. Since, on average, 43% and 38% of the LVOCs were properly condensing on aerosols in the O-OFR and I-OFR respectively, a correction was necessary and applied as in Eq. (2). (b) Fractional LVOC fates plotted vs OH exposure. (c) Fractional LVOC fates plotted vs average condensational sink (average of the input and output of the OFRs).

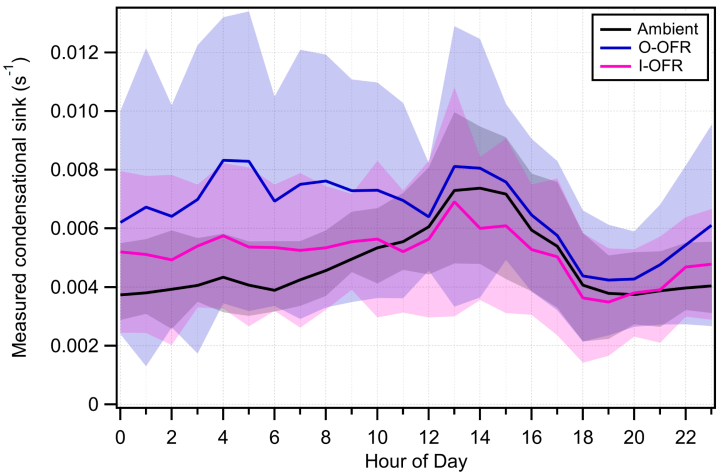

Figure S15. Average campaign diurnals of the measured condensational sink for ambient air, the output of the O-OFR and the output of the I-OFR, with shading representing one standard deviation. For the LVOC loss calculator, we estimated the condensational sink in each OFR by averaging the input (ambient air) and output condensational sink values.

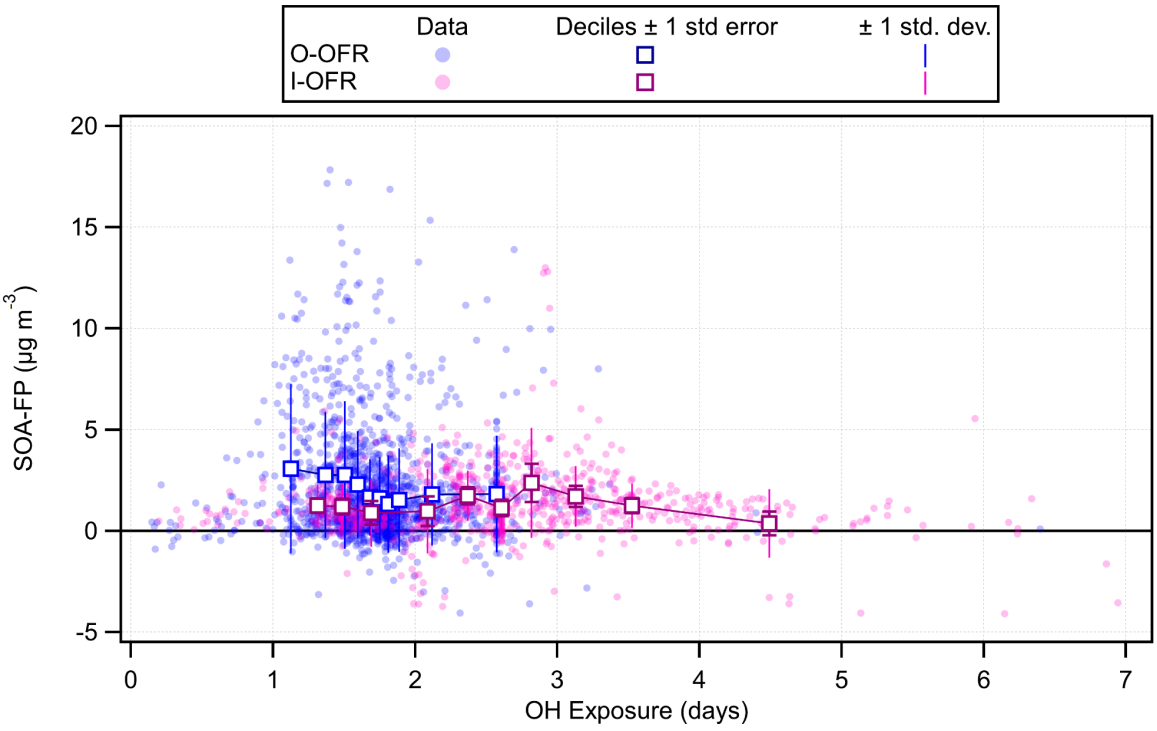

Figure S16. SOA-FP for both OFRs according to OH exposure (assuming a 24-h average OH concentration of 1.5 x 10^6 molec cm^{-3}). Deciles are shown as squares, with vertical error bars being the standard error (with caps). Some error bars are smaller than the markers. Standard deviations are shown as vertical lines (without caps). As discussed in the main text, no SOA formation dependence on OH exposure is expected or seen in this range of ages.

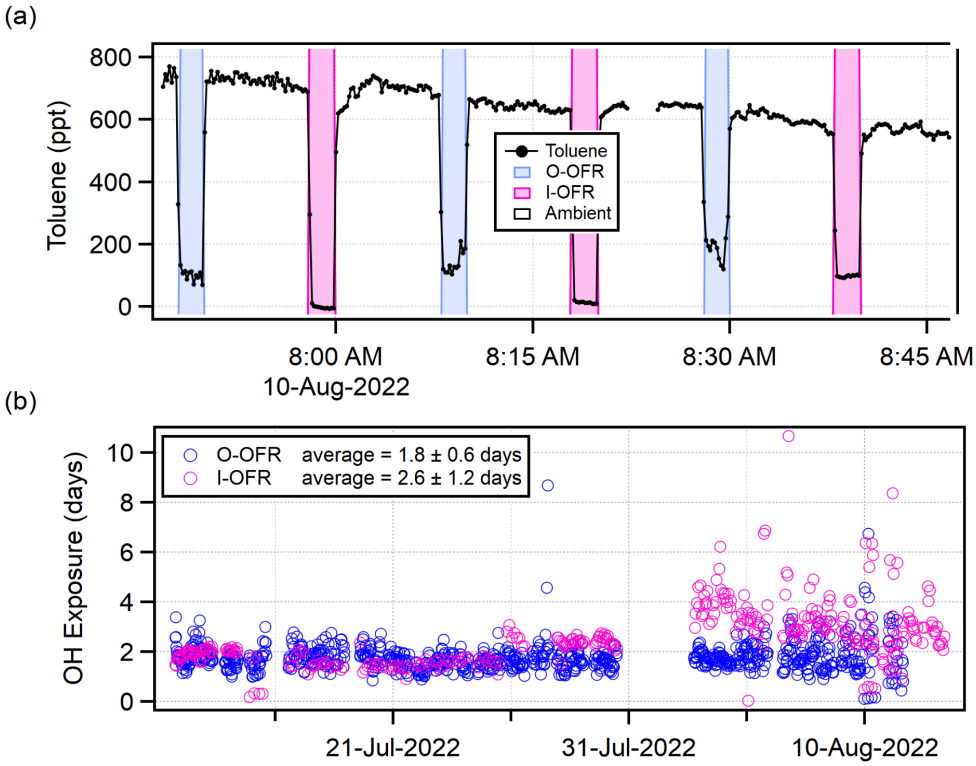

Figure S17. (a) A typical time series showing the decay of toluene in the OFRs compared to toluene in ambient air. (b) Calculated OH exposure (assuming a 24-h OH average concentration of 1.5 x 10^6 molec cm^{-3}) for each of the OFRs, in time. Averages are reported with one standard deviation.

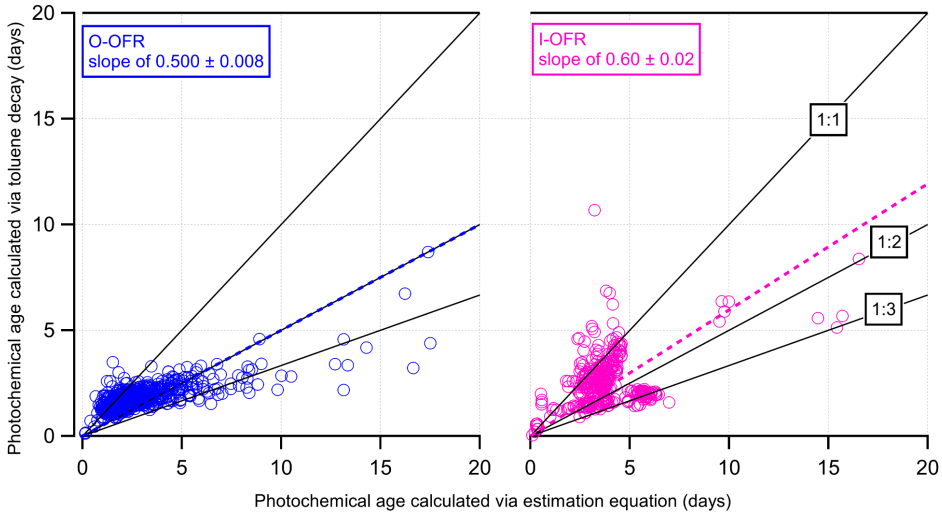

Figure S18. A comparison of OH exposures for both OFRs calculated from decays of toluene vs with the estimation equation from Li et al. (2015). The estimation equation results were used during the campaign to monitor the system, and the toluene decays were calculated post-campaign to refine the OH exposures.

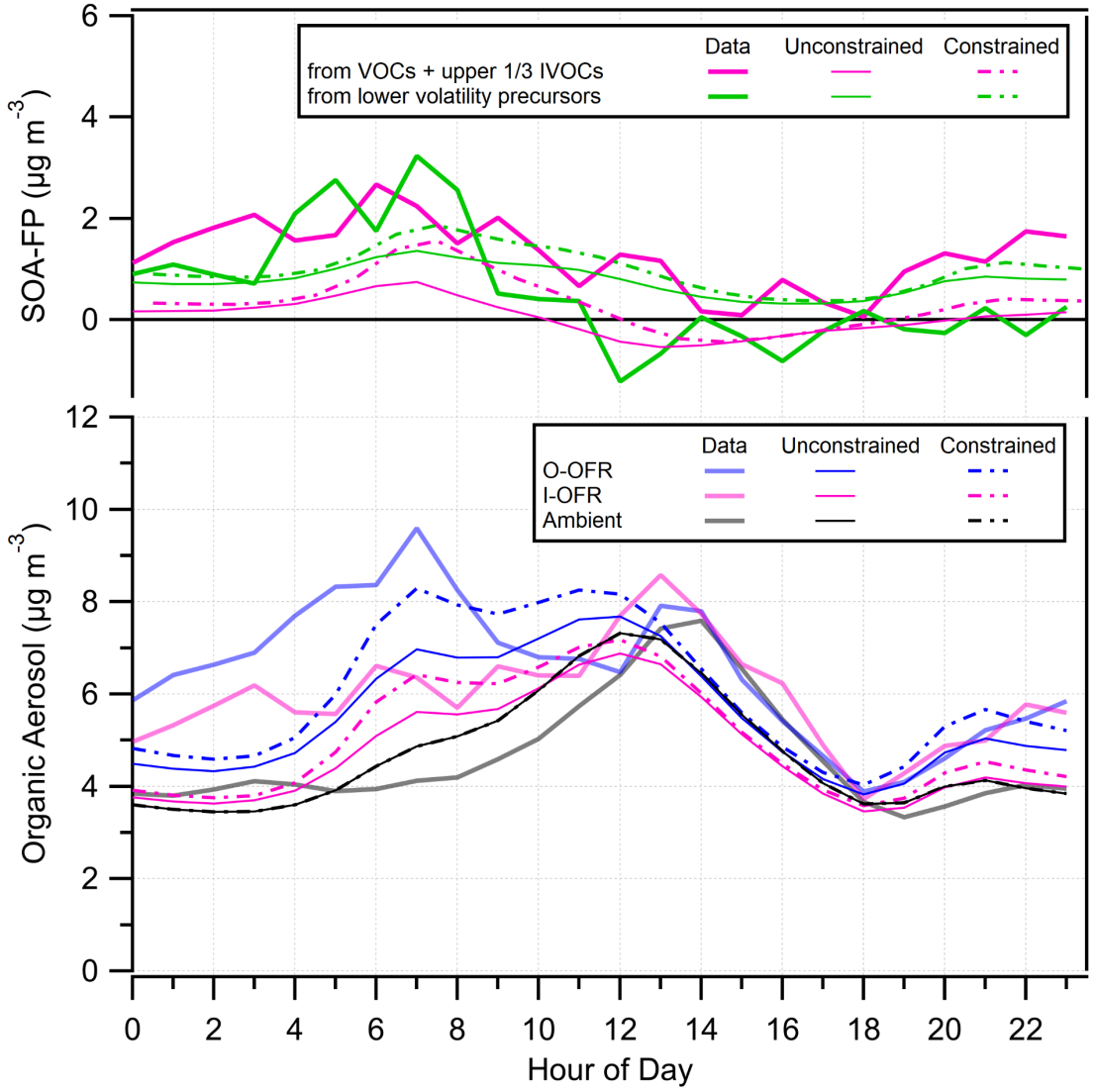

Figure S19. A modeling sensitivity study comparing CRACMM results when the input is unconstrained (raw CMAQ output) vs constrained (when Vocus measurements are used to constrain the CMAQ output, as is done in the main paper). Top: Campaign-averaged diurnal of SOA-FP according to the volatility split. Bottom: Campaign-averaged diurnal of total OA through the different sampling pathways.

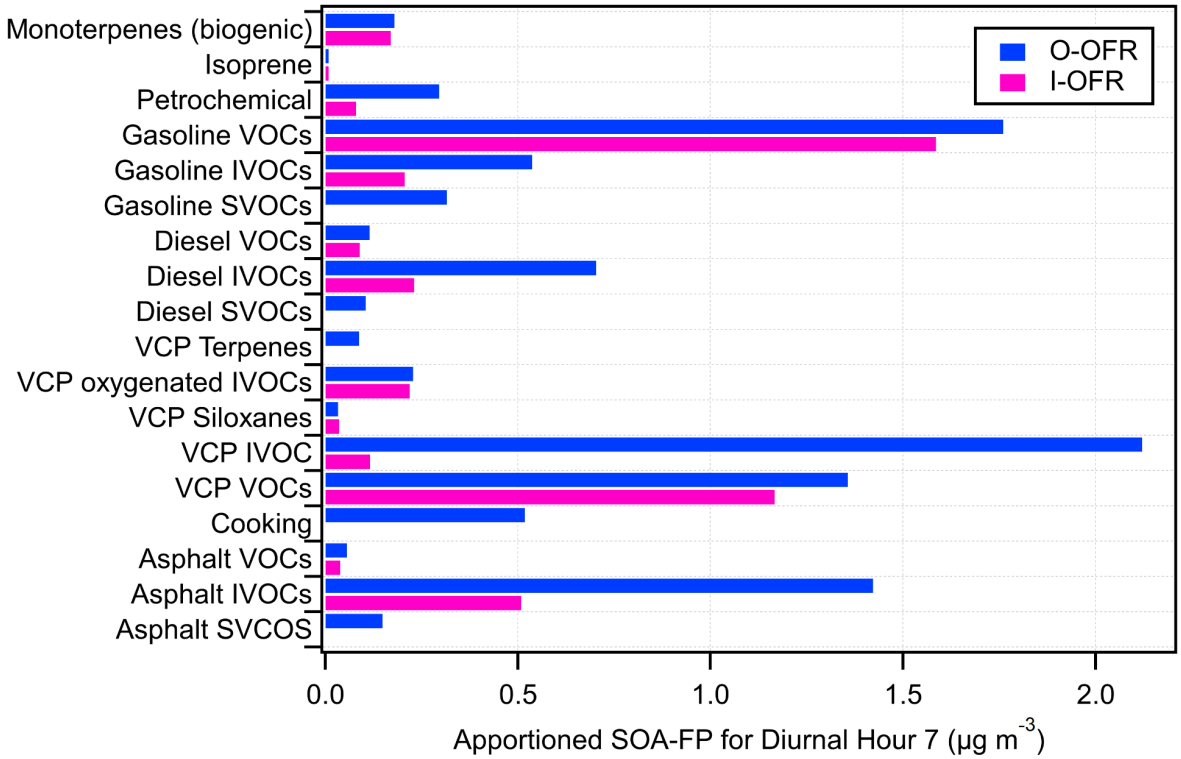

Figure S20. Breakdown of SOA-FP for diurnal hour 7 in the Caltech model according to sources and volatility. Contributions to ambient SOA have been subtracted off.

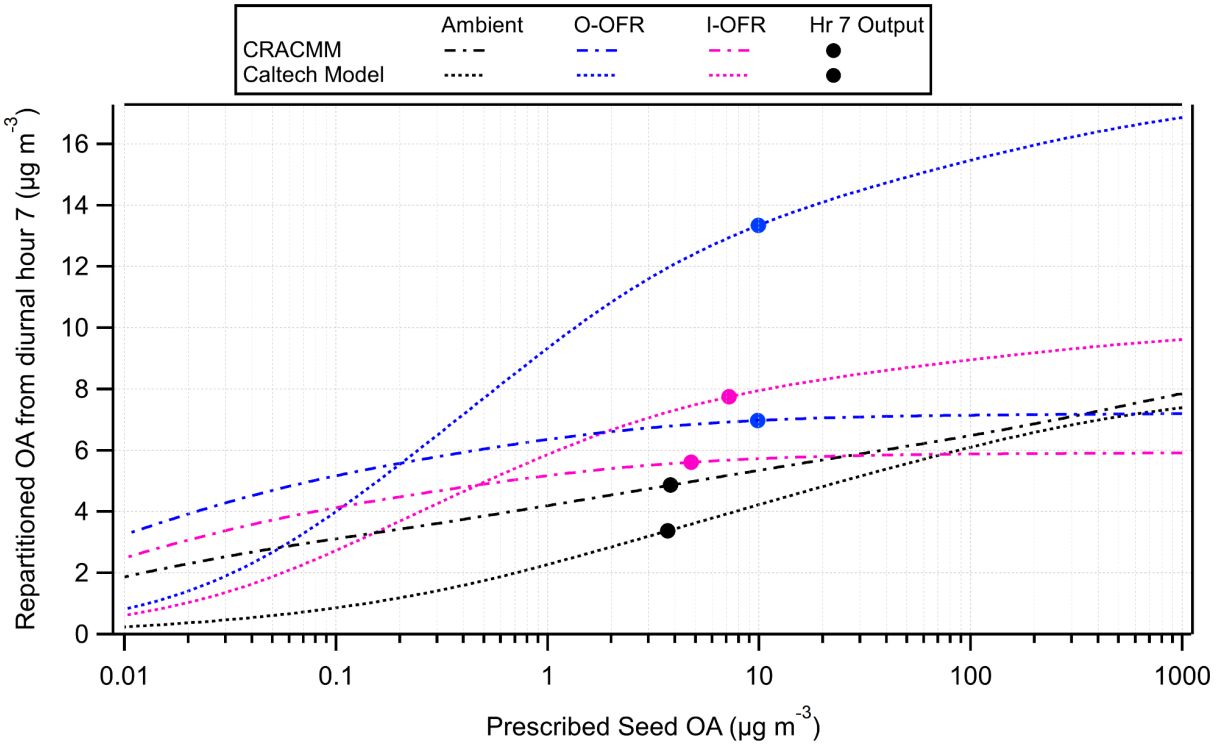

Figure S21. The total OA from diurnal hour seven (as indicated by the circle markers) was input into a separate model experiment, in which all chemistry was turned off and the OA was allowed to repartition according to a prescribed seed concentration, with a constant condensational sink of 1 s^{-1}. This calculation was done for both models for all three sampling pathways. By exposing the OA to lower prescribed seed OA concentrations we can quantify the amount of expected OA evaporation, and by exposing the OA to higher prescribed seed OA concentrations we can quantify the amount of expected OA condensation. This gives an indication of how sensitive each model is to evaporation and condensation. For example, if the OA from diurnal hour 7 of the ambient CRACMM model run was exposed to an order of magnitude less seed OA, only ~2 µg m^{-3} would evaporate, and conversely only ~0.5 µg m^{-3} would condense if the seed OA was increased by an order of magnitude.

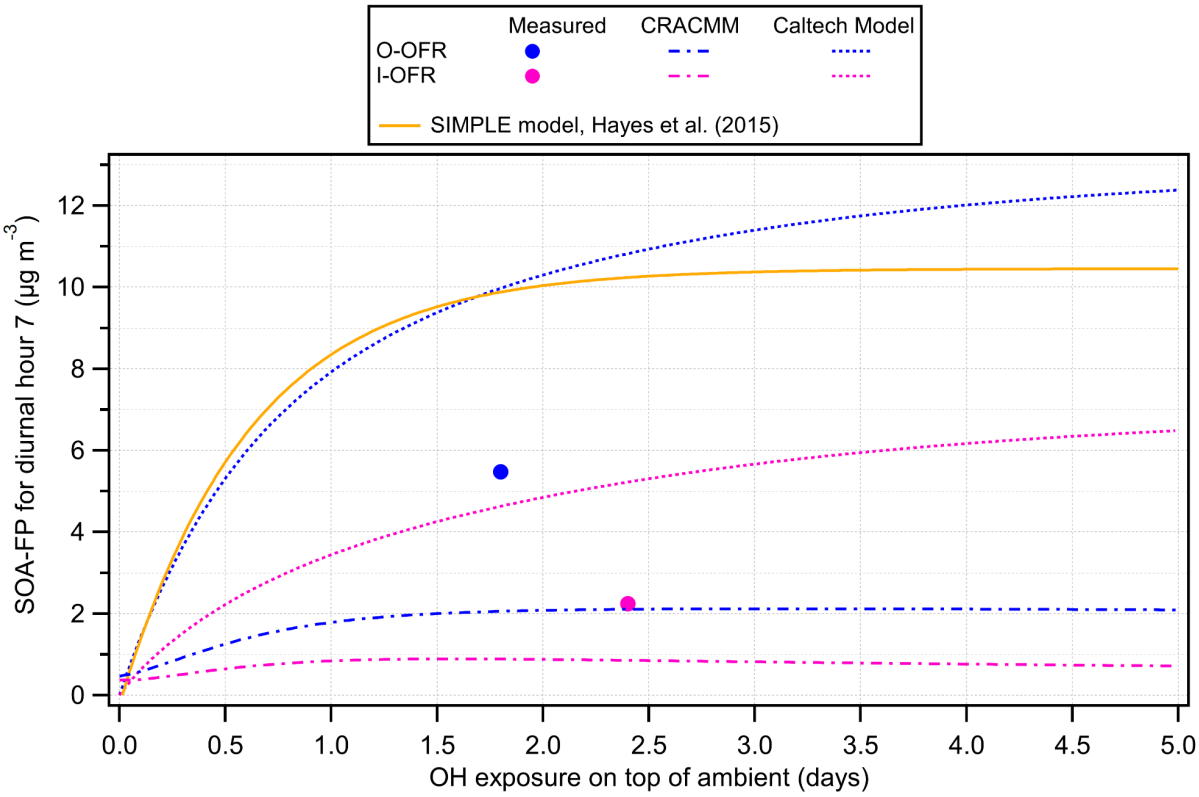

Figure S22. SOA-FP for diurnal hour seven as a function of photochemical age (on top of ambient age) for both models described in this work, the SIMPLE model from Hayes et al. (2015), and measurements. The ambient age determined in Jensen et al. (2024) for diurnal hour seven was 0.11 days, which has been subtracted on the x-axis.

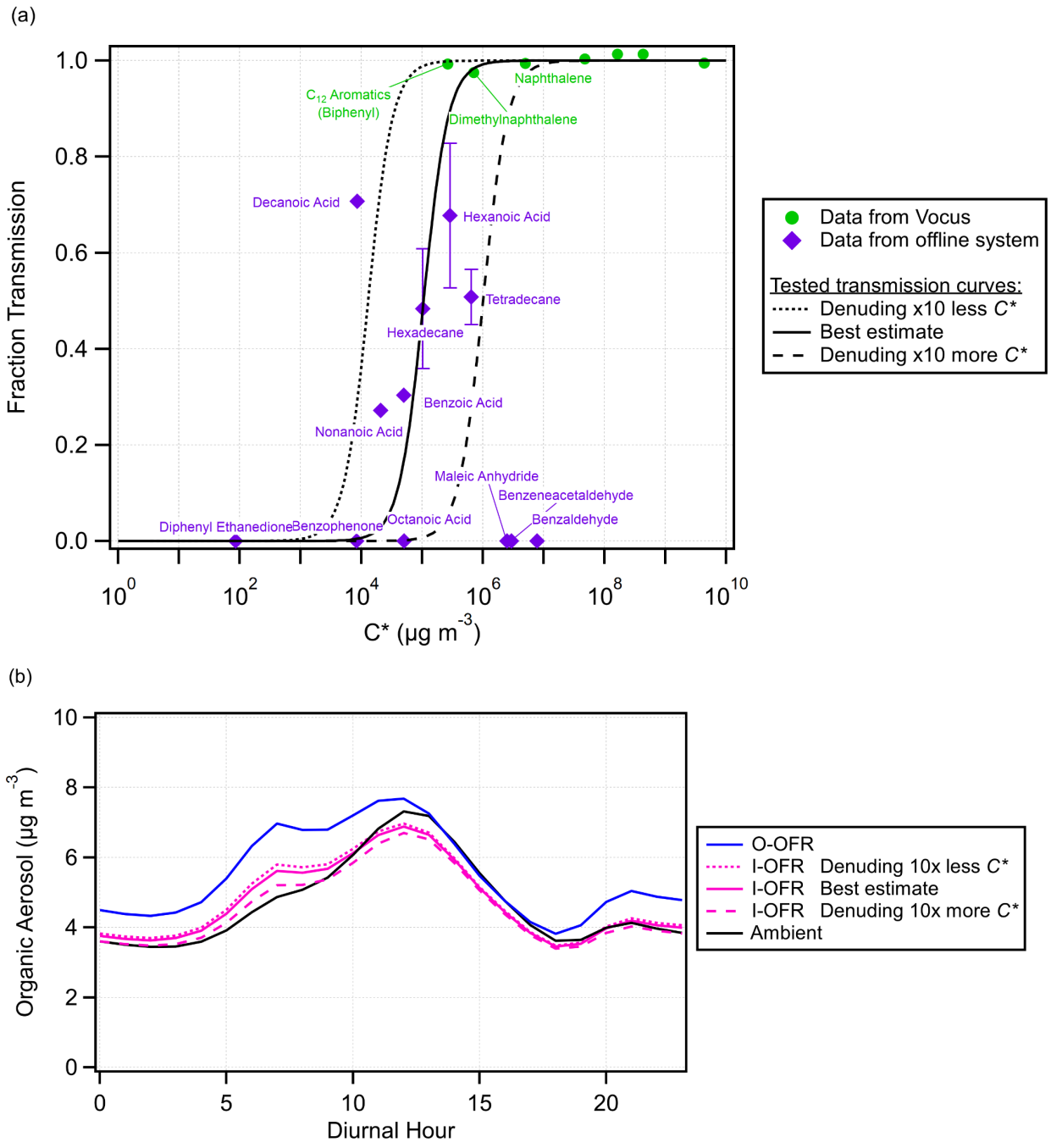

Figure S23. Sensitivity study for the CRACMM model to quantify the effect of shifting the volatility transmission curve on the modeled I-OFR OA. (a) The three transmission curves used for testing. (b) The resulting OA as a function of diurnal hour for the different transmission curves.

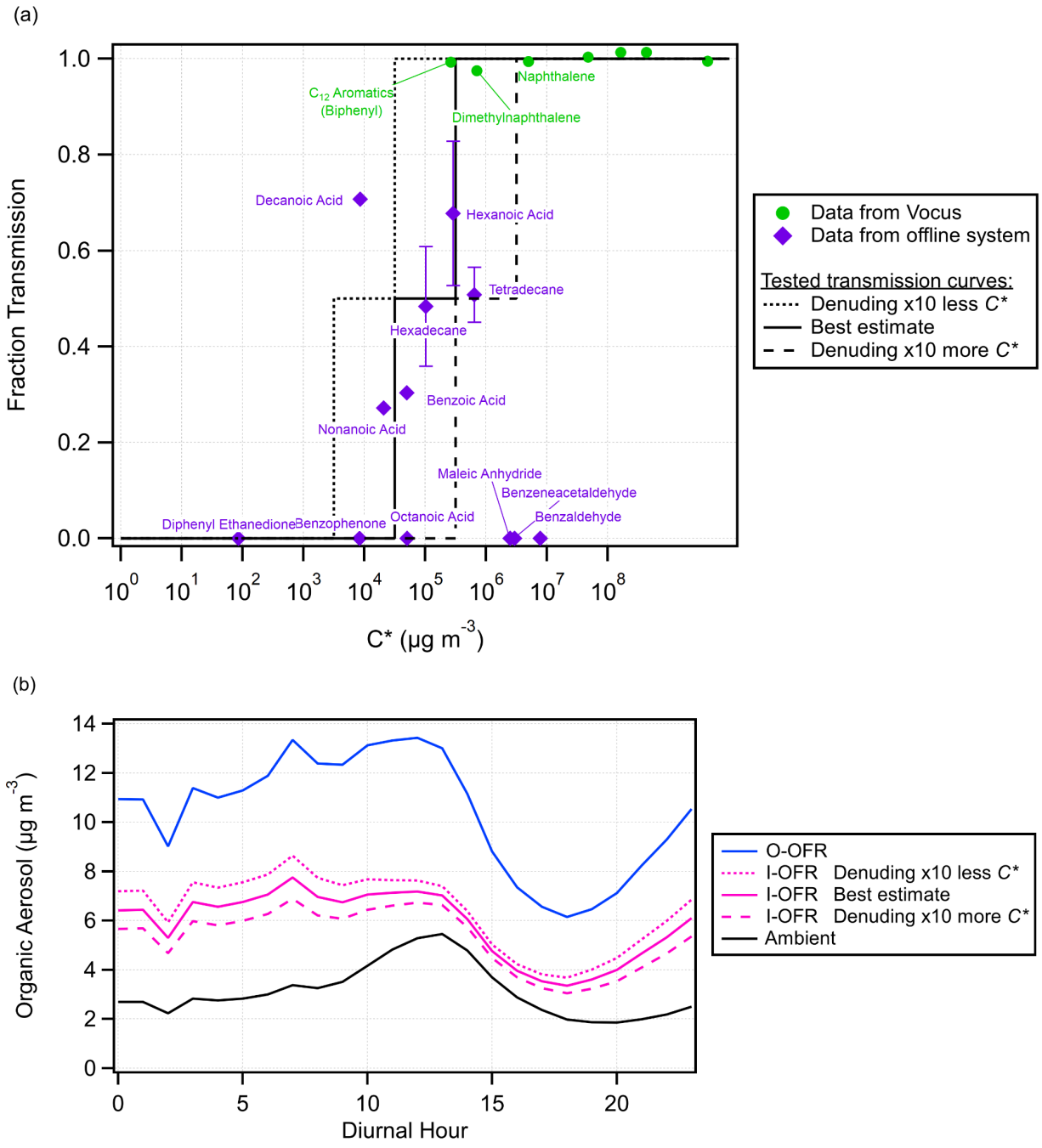

Figure S24. Sensitivity study for the Caltech model to quantify the effect of shifting the volatility transmission curve on the modeled I-OFR OA. (a) The three transmission curves used for testing. (b) The resulting OA as a function of diurnal hour for the different transmission curves.

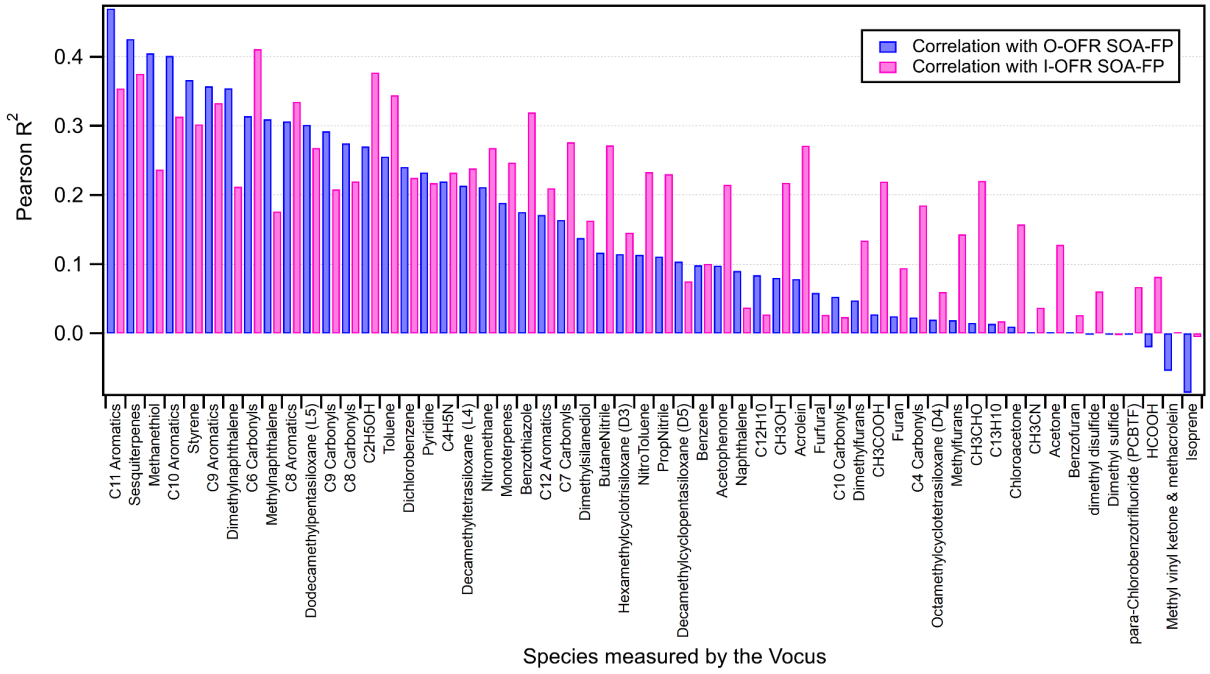

Figure S25. Bar chart showing Pearson R^2 values of all gas phase species (measured with the Vocus) with SOA-FP measured in each OFR.

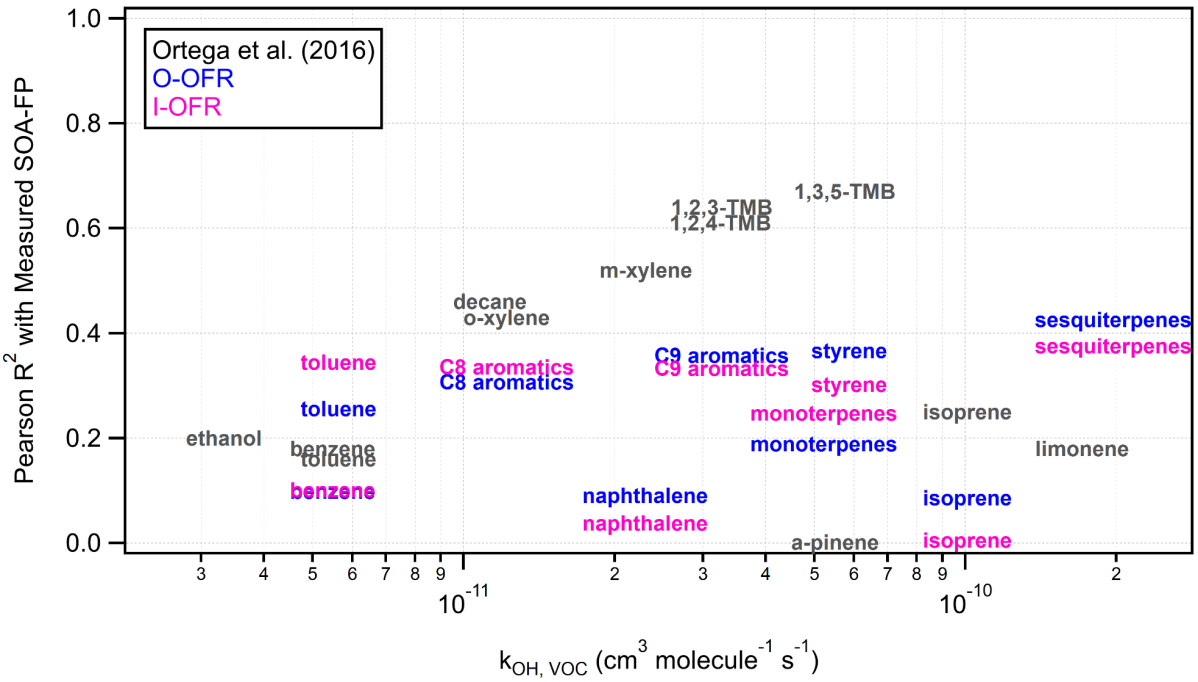

Figure S26. A comparison between 2022 and 2010 data (Ortega et al., 2016) showing correlations of VOCs with measured SOA-FP as a function of the rate coefficient constant for reaction with OH radicals. The formulas for C_8 and C_9 aromatics are C_8H_{10} and C_9H_{12} respectively.

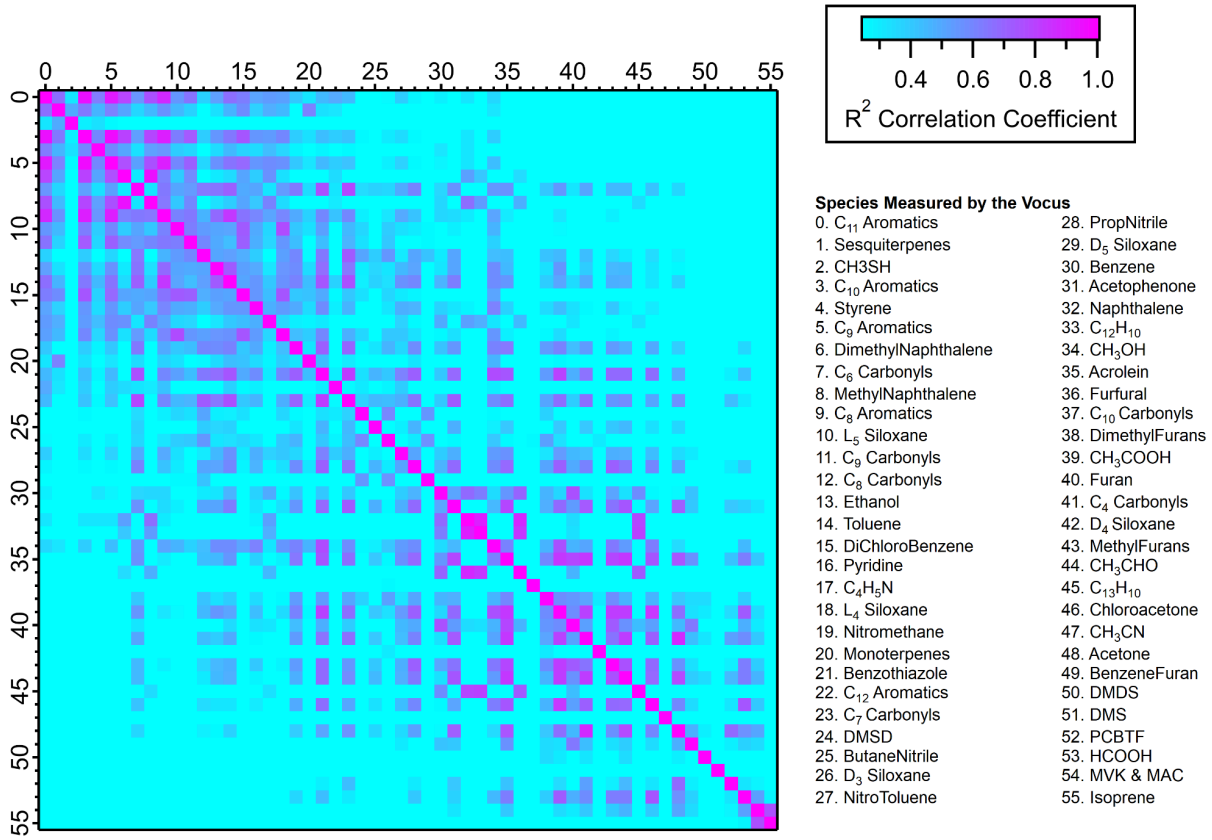

Figure S27. Matrix of Pearson R^2 values showing correlation between gas phase species measured by the Vocus in ambient air.

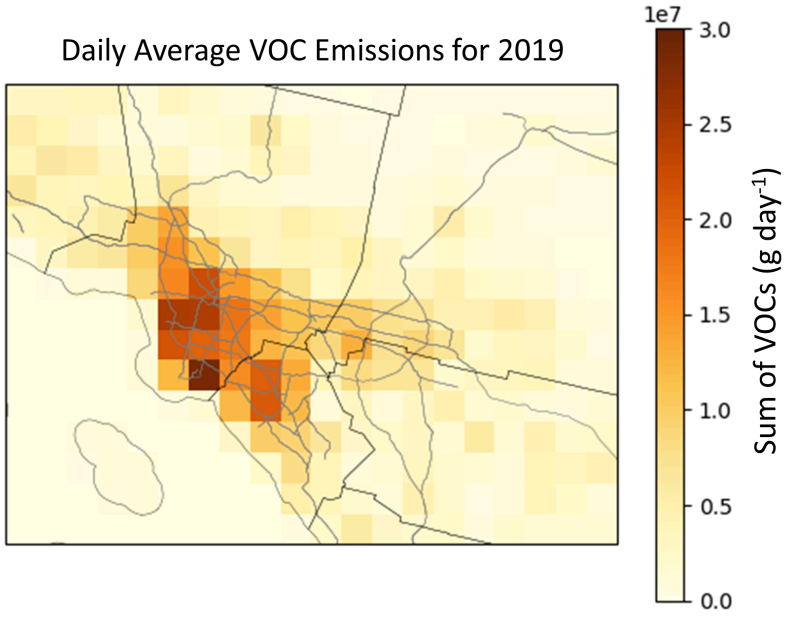

Figure S28. CMAQ model output of total VOC emissions for 2019 in the LA area.

	Ambient	All precursors	VOCs + ⅓ IVOCs	⅔ IVOCs + SVOCs
CRACMM	0.89	0.35	0.41	0.17
Caltech Model	0.76	0.80	1.36	0.19

Table S1. Slopes for the linear fits without a fixed intercept in Fig. 9.

Coef	Corresponding VOC (O-OFR)	Fit Coef. (μg m^{-3} ppt^{-1})	SOA mass yield from literature	Maximum SOA based on 7 am conc. (ug m^{-3})	Fit Coef. * conc. at 7 am (μg m^{-3})
a	C_{11} Aromatics	0.042	0.15[a]	0.013	0.61
b	Sesquiterpenes	0.045	1[b]	0.32	1.7
c	CH_3SH	0.22	-	-	1.7
d	Styrene	0.0050	0.023[c]	0.012	0.58
e	C_6 Carbonyls	0	0.013[a]	0.0035	0
	Corresponding VOC (I-OFR)	**Fit Coef. (μg m^{-3} ppt^{-1})**	**SOA mass yield from literature**	**Maximum SOA based on 7 am conc. (ug m^{-3})**	**Fit Coef. * conc. at 7 am (μg m^{-3})**
a	C_6 Carbonyls	0.0085	0.013[a]	0.0037	0.59
b	Ethanol	0	-	-	0
c	Sesquiterpenes	0.038	1[b]	0.33	1.5
d	C_{11} Aromatics	0	0.15[a]	0.013	0
e	Styrene	0.0049	0.023[c]	0.011	0.55

[a] McDonald et al. (2018), [b] Hoffman et al. (1997), [c] Schueneman et al. (2024), "-" no evidence of SOA formation

Table S2. Results for the VOC-SOA-FP regression from Eq. (3) for each OFR. The maximum SOA was calculated by converting the average concentration at 7 am for each precursor into mass, then multiplying by the reported literature yields (thus considering it reacts to completion with OH). The fit coefficients were multiplied by the average concentration at 7 am to calculate simulated SOA formation values. The maximum SOA values are much lower than the simulated SOA formation values, therefore, the precursors are understood as tracers. The precursors cannot make much SOA mass on their own, but can capture the variance of the SOA-FP throughout the day well, and represent all compounds that correlate with them.

References

Aiken, A. C., de Foy, B., Wiedinmyer, C., DeCarlo, P. F., Ulbrich, I. M., Wehrli, M. N., Szidat, S., Prevot, A. S. H., Noda, J., Wacker, L., Volkamer, R., Fortner, E., Wang, J., Laskin, A., Shutthanandan, V., Zheng, J., Zhang, R., Paredes-Miranda, G., Arnott, W. P., Molina, L. T., Sosa, G., Querol, X., and Jimenez, J. L.: Mexico city aerosol analysis during MILAGRO using high resolution aerosol mass spectrometry at the urban supersite (T0) – Part 2: Analysis of the biomass burning contribution and the non-fossil carbon fraction, Atmos. Chem. Phys., 10, 5315–5341, https://doi.org/10.5194/acp-10-5315-2010, 2010.

Hayes, P. L., Carlton, A. G., Baker, K. R., Ahmadov, R., Washenfelder, R. A., Alvarez, S., Rappenglück, B., Gilman, J. B., Kuster, W. C., de Gouw, J. A., Zotter, P., Prévôt, A. S. H., Szidat, S., Kleindienst, T. E., Offenberg, J. H., Ma, P. K., and Jimenez, J. L.: Modeling the formation and aging of secondary organic aerosols in Los Angeles during CalNex 2010, Atmos. Chem. Phys., 15, 5773–5801, https://doi.org/10.5194/acp-15-5773-2015, 2015.

Hoffmann, T., Odum, J. R., Bowman, F., Collins, D., Klockow, D., Flagan, R. C., and Seinfeld, J. H.: Formation of Organic Aerosols from the Oxidation of Biogenic Hydrocarbons, J. Atmos. Chem., 26, 189–222, https://doi.org/10.1023/a:1005734301837, 1997.

Jensen, A. R., Morris, M. A., Schulze, B. C., Bradley, A. C., Anderson, L. D., Jenks, O. J., Dresser, W. D., Ball, K., Ward, R. X., Day, D. A., Crounse, J. D., Meinardi, S., Barletta, B., Blake, D. R., Seinfeld, J. H., Wennberg, P. O., Jimenez, J. L., and de Gouw, J. A.: Emissions and chemistry of volatile organic compounds in the Los Angeles basin in summer 2022, J. Geophys. Res., 129, e2024JD041812, https://doi.org/10.1029/2024jd041812, 2024.

Li, R., Palm, B. B., Ortega, A. M., Hlywiak, J., Hu, W., Peng, Z., Day, D. A., Knote, C., Brune, W. H., de Gouw, J. A., and Jimenez, J. L.: Modeling the radical chemistry in an oxidation flow reactor: radical formation and recycling, sensitivities, and the OH exposure estimation equation, J. Phys. Chem. A, 119, 4418–4432, https://doi.org/10.1021/jp509534k, 2015.

McDonald, B. C., de Gouw, J. A., Gilman, J. B., Jathar, S. H., Akherati, A., Cappa, C. D., Jimenez, J. L., Lee-Taylor, J., Hayes, P. L., McKeen, S. A., Cui, Y. Y., Kim, S.-W., Gentner, D. R., Isaacman-VanWertz, G., Goldstein, A. H., Harley, R. A., Frost, G. J., Roberts, J. M., Ryerson, T. B., and Trainer, M.: Volatile chemical products emerging as largest petrochemical source of urban organic emissions, Science, 359, 760–764, https://doi.org/10.1126/science.aaq0524, 2018.

Nussbaumer, C. M. and Cohen, R. C.: Impact of OA on the temperature dependence of PM 2.5 in the Los Angeles basin, Environ. Sci. Technol., 55, 3549–3558, https://doi.org/10.1021/acs.est.0c07144, 2021.

Ortega, A. M., Hayes, P. L., Peng, Z., Palm, B. B., Hu, W., Day, D. A., Li, R., Cubison, M. J., Brune, W. H., Graus, M., Warneke, C., Gilman, J. B., Kuster, W. C., de Gouw, J., Gutiérrez-Montes, C., and Jimenez, J. L.: Real-time measurements of secondary organic aerosol formation and aging from ambient air in an oxidation flow reactor in the Los Angeles area, Atmos. Chem. Phys., 16, 7411–7433, https://doi.org/10.5194/acp-16-7411-2016, 2016.

Palm, B. B., Campuzano-Jost, P., Ortega, A. M., Day, D. A., Kaser, L., Jud, W., Karl, T., Hansel,

A., Hunter, J. F., Cross, E. S., Kroll, J. H., Peng, Z., Brune, W. H., and Jimenez, J. L.: In situ secondary organic aerosol formation from ambient pine forest air using an oxidation flow reactor, Atmos. Chem. Phys., 16, 2943–2970, https://doi.org/10.5194/acp-16-2943-2016, 2016.

Pfannerstill, E. Y., Arata, C., Zhu, Q., Schulze, B. C., Ward, R., Woods, R., Harkins, C., Schwantes, R. H., Seinfeld, J. H., Bucholtz, A., Cohen, R. C., and Goldstein, A. H.: Temperature-dependent emissions dominate aerosol and ozone formation in Los Angeles, Science, 384, 1324–1329, https://doi.org/10.1126/science.adg8204, 2024.

Schueneman, M. K., Day, D. A., Peng, Z., Pagonis, D., Jenks, O. J., de Gouw, J. A., and Jimenez, J. L.: Secondary organic aerosol formation from the OH oxidation of phenol, catechol, styrene, furfural, and methyl furfural, ACS Earth Space Chem., 8, 1179–1192, https://doi.org/10.1021/acsearthspacechem.3c00361, 2024.

Vettikkat, L., Miettinen, P., Buchholz, A., Rantala, P., Yu, H., Schallhart, S., Petäjä, T., Seco, R., Männistö, E., Kulmala, M., Tuittila, E.-S., Guenther, A. B., and Schobesberger, S.: High emission rates and strong temperature response make boreal wetlands a large source of isoprene and terpenes, Atmos. Chem. Phys., 23, 2683–2698, https://doi.org/10.5194/acp-23-2683-2023, 2023.